ACS Photonics

Article

pubs.acs.org/journal/apchd5

Diffractive Spectral-Splitting Optical Element Designed by Adjoint-Based Electromagnetic Optimization and Fabricated by Femtosecond 3D Direct Laser Writing

T. Patrick Xiao,[†,□] Osman S. Cifci,[‡,□] Samarth Bhargava,[†,#] Hao Chen,[‡] Timo Gissibl,[§] Weijun Zhou,[∥] Harald Giessen,[§] Kimani C. Toussaint, Jr.,[⊥] Eli Yablonovitch,[*,†] and Paul V. Braun[*,‡]

[†]Electrical Engineering and Computer Sciences Department, University of California, Berkeley, Berkeley, California 94720, United States

[‡]Frederick Seitz Materials Research Laboratory and [⊥]Department of Mechanical Science and Engineering, University of Illinois at Urbana−Champaign, Urbana, Illinois 61801, United States

[§]4th Physics Institute and Research Center SCoPE, University of Stuttgart, Pfaffenwaldring 57, 70569 Stuttgart, Germany

[∥]Core R&D − Materials Science, The Dow Chemical Company, Freeport, Texas 77541, United States

Supporting Information

ABSTRACT: The greatest source of loss in conventional single-junction photovoltaic cells is their inefficient utilization of the energy contained in the full spectrum of sunlight. To overcome this deficiency, we propose a multijunction system that laterally splits the solar spectrum onto a planar array of single-junction cells with different band gaps. As a first demonstration, we designed, fabricated, and characterized dispersive diffractive optics that spatially separated the visible (360−760 nm) and near-infrared (760−1100 nm) bands of sunlight in the far field. Inverse electromagnetic design was used to optimize the surface texture of the thin diffractive phase element. An optimized thin film fabricated by femtosecond two-photon absorption 3D direct laser writing shows an average splitting ratio of 69.5% between the visible and near-infrared light over the 380−970 nm range at normal incidence. The splitting efficiency is predicted to be 80.4% assuming a structure without fabrication errors. Spectral-splitting action is observed within an angular range of ±1° from normal incidence. Further design optimization and fabrication improvements can increase the splitting efficiency under direct sunlight, increase the tolerance to angular errors, allow for a more compact geometry, and ultimately incorporate a greater number of photovoltaic band gaps.

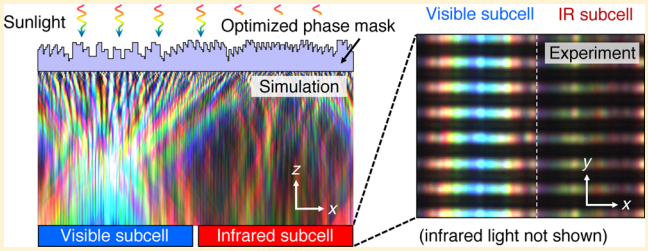

KEYWORDS: *multijunction photovoltaics, spectral splitting, diffractive optical element, adjoint optimization, inverse design, direct laser writing*

Fundamental loss mechanisms set an upper bound on the energy conversion efficiency of single-junction photovoltaic (PV) cells to 33.5% under one-sun illumination.[1] The most dominant source of loss is the broadband nature of sunlight, as contrasted with the relatively narrow energy range over which a PV cell efficiently converts energy; photons with energy smaller than the band gap fail to be absorbed, while photons with energy greater than the band gap lose their excess energy to heat via carrier thermalization. Multijunction devices have smaller thermalization losses and thus can more efficiently convert the full energy spectrum of solar radiation. Presently, the highest PV efficiencies are achieved by tandem structures, which use a stack of PV subcells with different band gaps.[2] However, tandem devices are costly to fabricate, as they generally require epitaxial growth of multiple layers of crystalline semiconductors as well as other processing steps. The tandem structure also imposes constraints on performance and design, as the different PV subcells must be current-matched. The current-matching requirement is of particular importance, as it imposes a strong sensitivity of PV efficiency on the shape of the solar spectrum, which varies with the Sun's position in the sky and with the chemical composition of the atmosphere, both of which will change with the time of day and time of year. As a result, the annual energy production from tandem devices does not necessarily improve proportionally with their high efficiency under the standard AM1.5 spectrum.[3−5]

An alternative multijunction architecture that decouples spectral filtering from photovoltaic conversion can potentially address these problems. Rather than growing the PV subcells in a vertical stack, they can instead be arranged in a lateral array. Each subcell can be independently grown, reducing cost and relaxing the material choice constraints, and independently connected, eliminating the current-matching constraint. A

Received: February 23, 2016
Published: April 25, 2016

DOI: 10.1021/acsphotonics.6b00066
ACS Photonics 2016, 3, 886−894

separate spectral-splitting optical element disperses the wavelengths of the incident sunlight, so that different bands of the solar spectrum are directed to subcells of matching band gaps. Spectral splitting has previously been implemented with prisms,[6] dichroic mirrors,[7] multiplexed volume holograms,[8] and specular reflection with highly selective interference filters.[9] However, the design freedom offered by spectral splitting using planar dispersive diffractive optics is particularly attractive for large-area PV applications, in similar fashion to thin dielectric surfaces proposed for light management in PV cells.[10]

Here we demonstrate spectral splitting using a planar diffractive optical element implemented as a surface texture on a dielectric material, as shown in Figure 1a. The surface

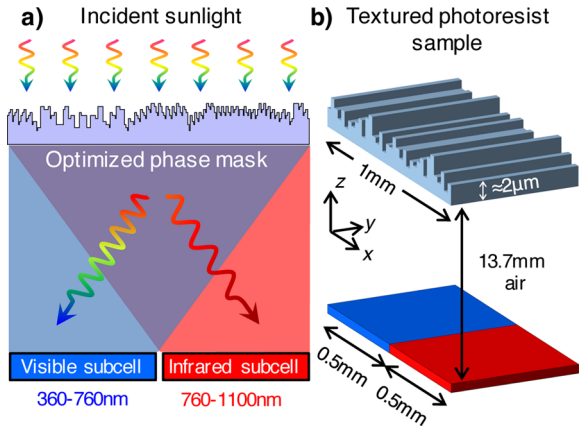

Figure 1. (a) A thin diffractive phase mask element is designed to laterally split the solar spectrum into two spectral bands and direct each band to separate partitions in the far-field image. (b) Diagram of the optical structure designed in this work showing geometric parameters.

texture is composed of flat top "pixels" of 5 μm lateral width, each of which imparts a controllable phase shift to the incident solar wavefront. If the height variation of the pixels is comparable in scale to the solar wavelengths, wavelengths on opposite extremes of the solar spectrum will undergo a significant difference in phase shift. Diffractive optical elements based on this principle have previously been demonstrated to produce distinct images in the far field when illuminated by various wavelengths of light.[11] The individual pixel heights in our texture are designed such that when the light propagates over a macroscopic distance to the far field, different spectral bands of light are directed to different spatial partitions of the image plane directly below the optical element. PV subcells can be placed in these partitions to complete the multijunction system. We note that this functionality involves both spectral dispersion and a mild amount of optical concentration, so that light incident on different positions of the phase mask are diffracted to different angles. Thus, our phase mask provides more flexibility in the position of the PV subcells over more traditional diffraction gratings that direct each color of light to a single diffracted order.[8]

Spectral-splitting elements of this type have been previously investigated using a photoresist material and a direct binary search algorithm to optimize the pixel height levels.[12,13] However, heuristic optimization methods require a very large number of simulations of the structure before arriving at an optimal solution. In this work, we present a method that exploits the reciprocity properties underlying Maxwell's equations to quickly obtain the gradient of the objective function with respect to the design variables (the individual pixel heights). Our approach, which we call the adjoint method, allows the optimization of electromagnetic structures with complex figures of merit at a much smaller computational cost compared to heuristic methods. The number of simulations required per iteration with this optimization approach does not scale with the number of design variables, allowing for the design of much larger or more complex structures without incurring an orders-of-magnitude increase in computational cost (i.e., number of simulations needed).

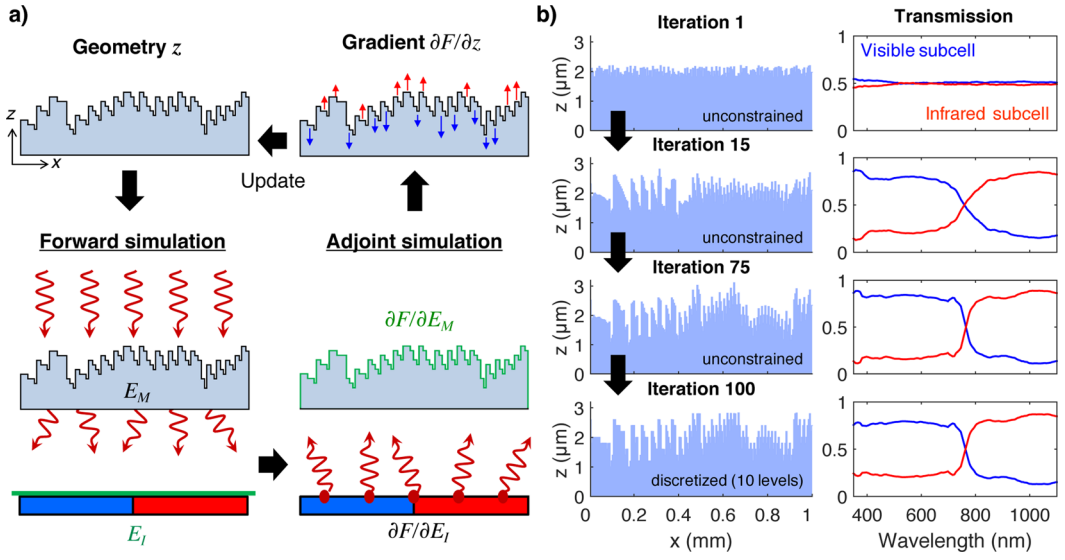

Figure 2. (a) An iteration of the optimization procedure involves a forward simulation of the structure to retrieve the far-field image and an adjoint simulation to compute the gradient of the figure of merit with respect to the design variables. The gradient is then used to make an iterative change to the structure. (b) Sample optimization showing the phase mask texture (left) and transmission coefficient into the visible and infrared image half-planes (right) throughout the optimization. After iteration 75, the height levels were constrained to yield a discretized final design.

DOI: 10.1021/acsphotonics.6b00066
ACS Photonics 2016, 3, 886−894

CONCEPT

There are many possible ways to optimize an electromagnetic structure. One strategy is to heuristically sample the design space until a solution is found that adequately performs the desired function. These methods are widely applicable and are commonly used.[13−15] However, complicated functionalities call for a complicated structure, which is necessarily described by a large number of design degrees of freedom. In these cases, heuristic methods are computationally cumbersome or infeasible to implement, due to the large number of physical simulations needed to explore a very large design space. Gradient-based optimization algorithms can circumvent this problem by finding a more direct path to a local optimum of the design space. However, a finite-difference calculation of the gradient still requires N simulations for each iteration of the design, one for each of N design variables used to specify the electromagnetic structure.[16] In this section, we show that the adjoint method in electromagnetics can reduce the cost of the gradient calculation to just *two* simulations per iteration; we call these the forward and adjoint simulations, as shown in Figure 2a. These methods have been successful in designing electromagnetic structures of various types.[16−20] Similarly to Scranton et al.,[18] we specifically analyze the case of optical diffraction to the far field (distance much greater than a wavelength). A more general treatment of the adjoint method for the optimization of electromagnetic structures can be found in refs 16 and 17.

We approximate the spectral-splitting element as a fully transmitting thin mask that modulates the phase of the incident wavefront. The phase mask is described by a surface texture (Figure 2a, top left), whose height at a particular position $\vec{r}_M$ in the mask plane M is specified by $z(\vec{r}_M)$. The scalar electric field E_M below the mask plane in response to an incident plane wave from air is

$$E_M(\vec{r}_M, \lambda, \hat{k}) = \exp\left[\mathrm{i}\frac{2\pi}{\lambda}(n(\lambda) - 1)\cdot z(\vec{r}_M) + \mathrm{i}\Phi(\lambda, \hat{k})\right] \tag{1}$$

where n is the refractive index of the mask material and $\Phi(\lambda, \hat{k})$ is the phase associated with a plane wave having a free-space wavelength λ and incidence direction $\hat{k}$. The parameter pair $(\lambda, \hat{k})$ identifies a single plane wave input, with the direction $\hat{k}$ specified by a polar angle θ and azimuthal angle ϕ with respect to the mask plane. At normal incidence ($\theta = 0$), $\Phi = 0$. Equation 1 is an accurate approximation if the mask is optically thin, the angle θ is small, and the lateral size of the design pixels is greater than a wavelength. Although the phase mask's response is calculated using eq 1 during the optimization to accelerate the design process, the exact electromagnetic response of the final design is evaluated using the finite-difference time-domain (FDTD) solution to Maxwell's equations. For a pixel size of 5 μm and wavelengths of 360−1100 nm used in this work, close agreement is found between eq 1 and the FDTD method.

We apply Huygens' principle to propagate the mask field E_M through free space to the image plane I, located at a distance $L \gg \lambda$ from the mask. Using the angular spectrum method of propagation,[21] the field E_I at a position $\vec{r}_I$ on the image plane can be expressed without approximation as a convolution integral:

$$E_I(\vec{r}_I) = \int_M E_M(\vec{r}_M)\cdot h(\vec{r}_I - \vec{r}_M)d^2\vec{r}_M \tag{2}$$

For convenience, we drop the input dependence $(\lambda, \hat{k})$ in our notation and provide the analysis for a single plane wave. M denotes the mask plane and $h(\vec{r}_I - \vec{r}_M)$ is the Green's function associated with the propagation of an electromagnetic point source along the vector $\vec{r}_I - \vec{r}_M$, which points from the mask to image. The field $E_M(\vec{r}_M)$ specifies the complex amplitudes of the point sources, distributed across the bottom surface of the phase mask. The computation of eq 2, which is shown schematically on the bottom left of Figure 2a, is vastly accelerated by evaluating the convolution integral using Fourier domain methods. Once E_I is obtained, the figure of merit F of the structure for a given plane wave input is found by evaluating a local objective function f across the image:

$$F = \int_I f[E_I(\vec{r}_I)]d^2\vec{r}_I \tag{3}$$

For spectral splitting, a simple choice for f is the optical intensity $|E_I(\vec{r}_I)|^2$ weighted by a binary function (either 0 or 1) at each position $\vec{r}_I$ that defines the desired region of the image plane for the transmission of a given wavelength. With this choice for f, F is proportional to the transmission coefficient through the desired region of the image. Finally, since sunlight is an incoherent source, a complete forward simulation requires evaluating eqs 1−3 once separately for each input wavefront $(\lambda, \hat{k})$ for which the mask is to be designed. The total electromagnetic figure of merit F_T is then obtained by summing over all of the input wavefronts: $F_T = \sum_{\hat{k}}\sum_{\lambda} F(\lambda, \hat{k})$. Schemes other than a sum can also be used to compute F_T that emphasize, for instance, the worst-performing input wavefront.

The derivative of the figure of merit with respect to the design variables $z(\vec{r}_M)$ is found by applying the chain rule. For a single plane wave,

$$\frac{\partial F}{\partial z(\vec{r}_M)} = 2\,\mathrm{Re}\left(\frac{\partial F}{\partial E_M(\vec{r}_M)}\frac{\partial E_M(\vec{r}_M)}{\partial z(\vec{r}_M)}\right) \tag{4}$$

where we have used the fact that F is real-valued. The second term on the right side can be found easily using eq 1. The first term is expressed by differentiating eq 3, again applying the chain rule. The result is:

$$\frac{\partial F}{\partial E_M(\vec{r}_M)} = \int_I \frac{\partial f}{\partial E_I(\vec{r}_I)}h(\vec{r}_M - \vec{r}_I)d^2\vec{r}_I \tag{5}$$

Here, we have invoked the well-known reciprocity of electromagnetic Green's functions, which expresses the principle that any optical path between two points is identical in either direction, a property of Maxwell's equations first recognized by Poynting[22] and Lorentz.[23] This implies that the same Green's function h can be used to propagate an electric field in both the forward direction (mask to image, $\vec{r}_I - \vec{r}_M$) and the reverse direction (image to mask, $\vec{r}_M - \vec{r}_I$):

$$h(\vec{r}_I - \vec{r}_M) = h(\vec{r}_M - \vec{r}_I) \tag{6}$$

This equivalence can also be seen directly from the expression for the propagation Green's function h in diffractive optics.[21]

DOI: 10.1021/acsphotonics.6b00066
ACS Photonics 2016, 3, 886−894

Equation 5 is completely analogous to eq 2, except that the propagation is from the image to the mask, and the point sources are defined on the *image* plane with complex amplitudes $\partial f/\partial E_I(\vec{r}_I)$. We thus have the result that the calculation of the gradient on the left side of eq 5 can be reduced to a single physical simulation from the image to the mask, as illustrated in Figure 2a, bottom right. We call this the *adjoint* simulation, so named because this method is an instance of the more general adjoint (or dual) method in linear algebra.[16,17] The adjoint simulation provides the gradient of F with respect to *all* N variables, regardless of the size of N. This key advantage makes our gradient-based approach highly scalable, allowing for efficient optimization of structures with a large number of design variables. Additionally, an arbitrarily complex function f can be chosen as the optimization figure of merit, provided that the expression for f can be differentiated to obtain the complex amplitudes $\partial f/\partial E_I(\vec{r}_I)$ in the adjoint simulation.

As for the case of the forward simulation, a complete adjoint simulation requires eqs 4 and 5 to be evaluated once for each input wavefront $(\lambda, \hat{k})$. To calculate the gradient of the total figure of merit F_T, the gradients for the individual inputs are summed: $\partial F_T/\partial z = \sum_{\hat{k}} \sum_{\lambda} \partial F(\lambda, \hat{k})/\partial z$. If a scheme other than a sum over inputs is used to evaluate F_T, the expression for F_T must be carefully differentiated to obtain the total gradient. These schemes were not used to produce the final design in this work.

In practice, the pixel heights $z(\vec{r}_M)$ in the spectral-splitting texture cannot be adjusted with infinite precision. With the fabrication capabilities available to produce such an element, a multilevel structure is more realistic, in which all of the pixel heights $z(\vec{r}_M)$ in the design are selected from a small number of discrete height levels with constant spacing. Rather than explicitly discretizing the pixel heights in the optimization, we continue to treat $z(\vec{r}_M)$ as a continuous variable and include an additional term in the figure of merit expression to penalize F_T if the height $z(\vec{r}_M)$ does not belong to a set of allowed height values. This step requires no new simulations. The relative weights of the electromagnetic merit function and the constraint function can be adjusted so that neither value suffers significantly during the constrained optimization (see Supporting Information for more details).

Once the gradient $\partial F_T/\partial z$ is known, various algorithms are available to find the optimal update to the geometry Δz (Figure 2a, top right). In this work, we use the steepest descent algorithm, which gives an update Δz that is proportional to the gradient. The constant of proportionality, or optimization step size, is found using a line search algorithm.[24] After the update is made, the forward and adjoint simulations are performed on the new geometry to calculate the next update. This iterative process is continued until a convergence condition is met. If sufficient memory is available for the computation, the geometry update can also be calculated from the gradient information using a quasi-Newton method to obtain faster convergence.[24] This was not implemented to produce the main optimization result in this work.

RESULTS AND DISCUSSION

Figure 1b shows the geometric parameters chosen for the spectral-splitting element designed in this work. The surface texture of the thin film is discretized to 10 equally spaced height levels spanning a range of 1.8 μm in steps of 0.2 μm. The texture's height is modulated along x with a pixel width of 5.0 μm, so that one period of the design contains 200 pixels over a total length of 1.0 mm. The height is constant in the y direction. In our experiment, the light propagates through a 13.7 mm air gap after passing through the thin photoresist film. Alternatively, the texture can also be patterned on the top surface of an optically thick dielectric or polymer slab that rests directly on top of the photovoltaic cells.

The design was optimized for 127 wavelengths over the range of 360 to 1100 nm, which contains about 81% of the power in the AM1.5D solar spectrum.[25] Wavelengths shorter than the chosen cutoff of 760 nm (roughly corresponding to the band of visible light) were directed to one half of the image plane as shown in Figure 1a, and wavelengths longer than 760 nm (near-infrared light) were directed to the other half-plane. We henceforth refer to these half-planes as the visible and infrared subcells, respectively, following the placement of the PV subcells in the image plane shown in Figure 1a. The structure in this work was optimized for normal incidence only. As the figure of merit, we define the design's spectral-splitting efficiency as

$$\text{Spectral splitting efficiency} \equiv \frac{1}{N_\lambda} \sum_i \left[T_{\text{vis}}(\lambda_i) \times (\lambda_i \le 760\ \text{nm}) + T_{\text{IR}}(\lambda_i) \times (\lambda_i > 760\ \text{nm}) \right] \tag{7}$$

where N_λ is the number of wavelengths sampled for the efficiency calculation, T_{vis} is the transmission coefficient through the visible subcell, and T_{IR} is the transmission coefficient through the infrared subcell. The optimal solution should transmit nearly all of the incident visible light (λ < 760 nm) to the visible subcell and nearly all of the incident infrared light (λ > 760 nm) to the infrared subcell, with a sharp transition between the subcells near the cutoff of λ = 760 nm. In keeping with the goal of large-area photovoltaic power conversion, the structure was optimized assuming periodic boundary conditions along x and extended infinitely along y.

The optimization was performed in two phases. Starting from a randomly generated texture, an unconstrained optimization was first performed to obtain a high spectral-splitting efficiency. After the first phase of unconstrained optimization, we impose the discretization constraint to yield a final structure with 10 discrete height levels. The first phase of the optimization was run for 75 iterations, and the second phase was run for 25 iterations, for a total of 200 physical simulations through the entire design process using the adjoint method. Both the simulation and optimization steps were written using MATLAB scripts, and the design process took less than 2 min on a single machine using two 3.2 GHz processors.

The optical performance at several points during the optimization process is shown in Figure 2b for a representative design. The optimization algorithm requires only a few iterations to reach a design that efficiently splits the wavelengths to the desired cells, as shown by the performance at iteration 15, then continues to refine the design as it approaches the local optimum at iteration 75. Since the structure is specified by 200 pixel heights, each of which is an independent design variable, many high-performing local optima exist even when the design is constrained. Therefore, the splitting efficiency does not substantially deteriorate during

DOI: 10.1021/acsphotonics.6b00066
ACS Photonics 2016, 3, 886−894

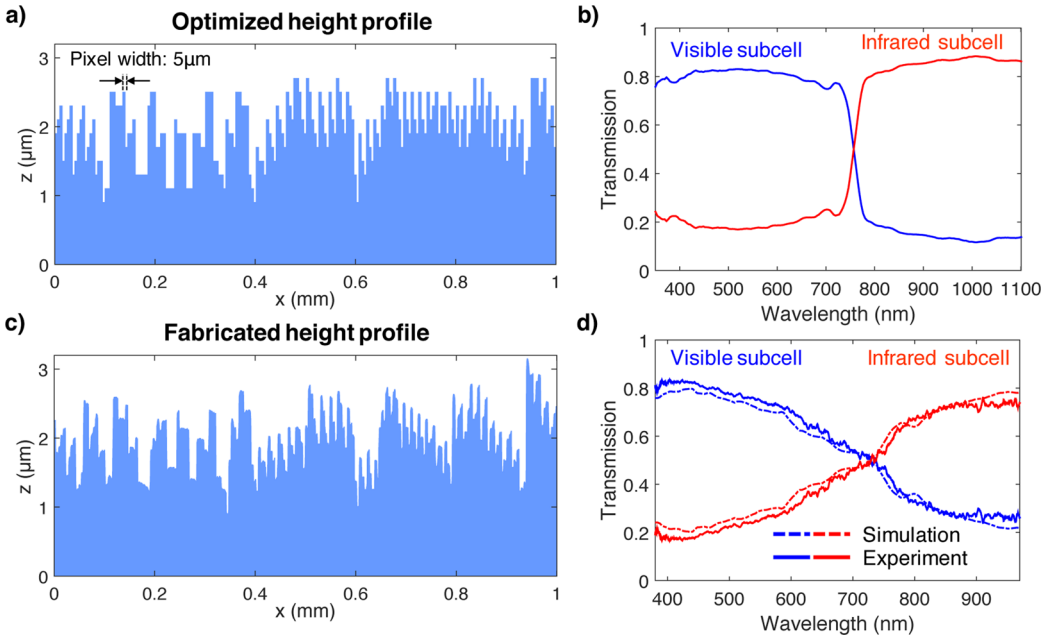

Figure 3. (a) Height profile for the final result of the computational optimization. (b) Simulated spectral response of the optimized design. (c) Height profile of one period of the fabricated sample, measured using confocal microscopy. (d) Simulated (dotted) and experimentally measured (solid) spectral performance of the fabricated structure.

the constrained optimization step to produce a 10-level structure (iterations 76 to 100).

The optimal mask texture found using the adjoint method is shown in Figure 3a. To evaluate the spectral-splitting efficiency of this design, the near-field response of the structure is evaluated using FDTD methods, and the calculated fields are propagated to the far field using scalar diffraction methods. To enable comparison of the optimized structure with experimental results, periodic boundary conditions were not assumed. For a feature size of 5 μm and a distance of 13.7 mm, about ∼87% of the optical power transmitted through one phase mask period is diffracted into its own image plane (directly underneath) or to the image planes of its two nearest neighbors along x. Therefore, to approximately replicate the periodic boundary conditions in the experiment, it is sufficient to produce a system with three repeated 1 mm phase masks and measure the response at the image plane directly beneath the central period. This situation was simulated in the propagation step, with the transmission coefficients in eq 7 normalized to the power received by the central image plane. Since a small amount of the incident light is diffracted to large angles beyond the nearest-neighbor image planes, this calculated efficiency will slightly overestimate the spectral-splitting efficiency of a true infinitely periodic system.

Under these considerations, the spectral response of the final design is shown in Figure 3b, predicting a spectral-splitting efficiency of 81.5% over the full design range of 360−1100 nm. The efficiency of this design over the spectral range of our characterization instruments (380−970 nm) is 80.4%. We also note that the spectral-splitting efficiency predicted using eq 1 for the near-field response deviates from the result of the FDTD simulation by <1% (absolute difference), validating the accuracy of the thin mask approximation used to accelerate the optimization process.

A sample (Figure 4a) containing three periods of the phase mask specified in Figure 3a was fabricated using femtosecond 3D direct laser writing with IP-Dip photoresist. The laser writing system produces the textured photoresist sample in a single three-dimensional scan without requiring multiple masks or alignment steps and achieves submicrometer structural resolution by exciting nonlinear optical processes in the photoresist material.[26] We note that multiphoton laser writing remains a viable fabrication option even for submicrometer lateral pixel dimensions should such pixels be required for future spectral-splitting designs. The total area of the fabricated sample is 3 mm (x) × 2.4 mm (y), formed by stitching together individually written regions that have a length of 0.15 mm along y (see stitching lines in Figure 4b). The height profile of the central period, measured using confocal microscopy, is shown in Figure 3c. Although many of the important features of the optimized height profile are reproduced, the individual pixels in the fabricated sample are not completely flat, and both pixel heights and widths exhibited some deviations from the design values.

The optical response of the phase mask was characterized using the setup shown in Figure 5. A broadband light source was collimated using an achromatic lens to reproduce the normal incidence beam assumed during the optimization. To uniformly illuminate only the area of the phase mask, an aperture of the same dimensions as the sample was placed before the sample to define the incident beam. Visual inspection of the image plane reveals that spectral splitting is taking place. Figure 4c shows the image plane (of the full three periods of the sample) captured by a color CCD camera with a built-in infrared filter. Much of the transmitted visible light is split to one-half of the image, with some undesired visible light arriving on the infrared side. The dark horizontal fringes in the image, separated by 0.15 mm in y, are an artifact of imperfections in the direct laser writing process. Along the y direction, the individually written areas of the phase mask are not completely flat but rather have a small tilt. This leads to small offsets in the sample's height profile at the stitching boundaries (visible in Figure 4b), which are separated by 0.15 mm. The tilted profile with periodic height offsets form a

DOI: 10.1021/acsphotonics.6b00066
ACS Photonics 2016, 3, 886−894

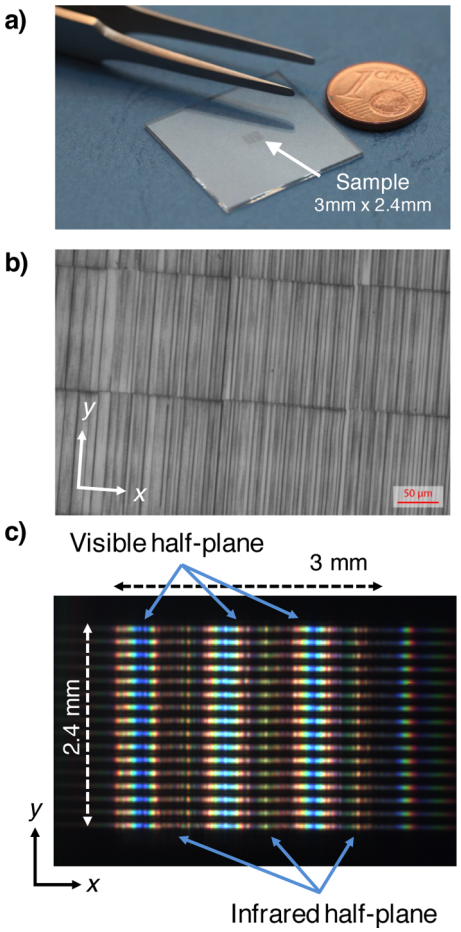

Figure 4. (a) Photograph of the fabricated phase mask sample. (b) Scanning electron microscopy (SEM) image of a portion of the sample, showing 5 μm wide strips of constant height. Dark horizontal lines mark the separation between stitched areas. (c) Visible CCD image of the sample in the far field, showing lateral splitting of the spectrum from three periods of the phase mask texture.

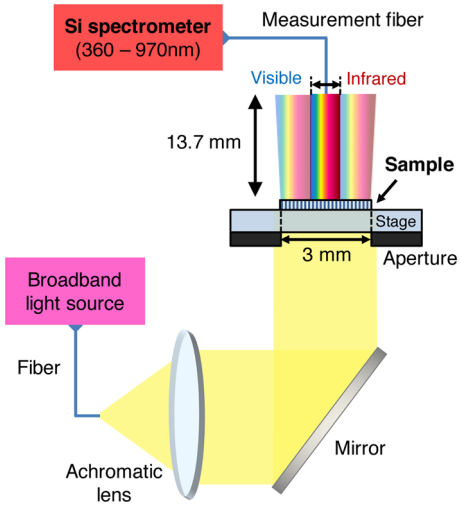

Figure 5. Schematic of the optical characterization experiment.

blazed phase grating in the y direction, which produces the bright and dark fringes in the far-field image. A more precise fabrication process can eliminate this fringe pattern.

The spectral-splitting efficiency was measured by scanning a measurement fiber across the image plane of the central period of the sample (along the x direction). The fiber tip has a diameter of 50 μm, and accordingly the output light was collected at 50 μm steps of the fiber tip x-position and transmitted through the fiber into a photodiode array spectrometer. The solid curves in Figure 3d plot the measured performance of the fabricated sample over the operational range of the spectrometer (380–970 nm). The experimentally observed splitting efficiency of the fabricated sample over this spectral range is 69.5%.

The dashed curves in Figure 3d show the simulated response of the fabricated sample. The simulation methodology is the same as that used to produce Figure 3b, but now uses the measured height profile in Figure 3c rather than the computationally optimized profile in Figure 3a to evaluate the combined effect of all types of fabrication errors. Additionally, the simulation accounts for the circular shape and discrete positions of the measurement fiber (this affects the splitting efficiency by <1%). The simulated and experimental results show close agreement; averaged over 380–970 nm, the absolute difference in transmission into the desired cell is ±3.1% between the simulation and experiment. Compared to the performance of the computationally optimized design over the same spectral range, the observed spectral-splitting efficiency is reduced by 10.9%. The efficiency drop is manifested mostly in the reduced sharpness of the splitting transition from the visible cell to the infrared cell, while the peak splitting ratios on the two sides of the splitting transition are not significantly degraded. The agreement of the simulation and experiment in Figure 3d suggests that fabrication errors are mainly responsible for the degraded performance relative to the optimization result.

Equation 1 predicts that the phase response of the sample is polarization-independent, which rests on the assumption that the texture is locally flat to the incident light. When this holds, the structure's responses to the different vector components of the electric field are not coupled.[20] In evaluating eq 1, this condition is satisfied by assuming a pixel width that is several times larger than the wavelength. FDTD simulations of the fabricated structure in response to light polarized along and orthogonal to the design direction (x) show less than a 0.1% absolute difference in spectral-splitting efficiency (under normal incidence, 380–970 nm). Experimental results also show insensitivity to incident polarization. The sample's spectral response in Figure 3d was characterized using a broadband, unpolarized light source. Separate measurements that filter one of the two polarizations show that the sample's spectral-splitting efficiency under either polarization differs from the case of unpolarized light by no more than 0.33% (see Supporting Information). Since sunlight is also unpolarized, this lack of polarization sensitivity is advantageous for solar energy harvesting.

Neither the simulated nor measured spectral-splitting efficiency accounts for light that is lost while traveling through the system. FDTD simulations of the fabricated structure in Figure 3c predict the transmittance through the phase mask to be 91.4%, averaged over the two polarizations and weighted by the power spectrum of the light source. This loss can be explained by Fresnel reflections from the two air–photoresist interfaces in the sample. Experimentally, the transmittance through the sample is found to be 89.5%, by comparing the power measured at the sample surface and the power collected

DOI: 10.1021/acsphotonics.6b00066
ACS Photonics 2016, 3, 886–894

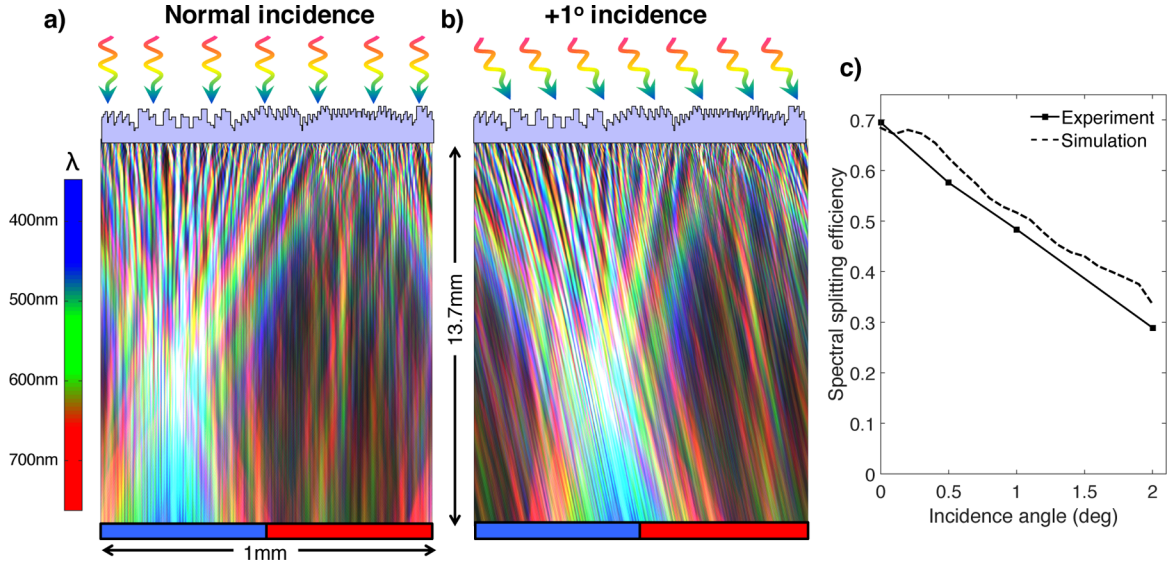

Figure 6. (a) Colored profile of the simulated optical intensity between the sample and the image plane, under normal-incidence illumination with wavelengths of 360−760 nm. The color at a point in space denotes the wavelengths with large relative flux density in that region, following the color scheme on the left. (Wavelengths corresponding to different colors are added using their RGB color values.) (b) Intensity profile under collimated illumination from a +1° polar angle. (c) Spectral-splitting efficiency vs incidence angle, averaged from 380 to 970 nm.

over the image plane. The deviation between simulation and experiment is within the measurement uncertainty of the power sensors.[27] As would be required for a high-efficiency PV system, the reflection losses may be reduced by replacing the air gap with a dielectric layer index-matched to the phase mask, eliminating one of the two reflective interfaces, and with the addition of an antireflection coating on the top surface of the phase mask.

Under solar irradiation, an important additional consideration is the angle of the incident light. Although the collimated light in our experiment has negligible angular spread, the Sun subtends an angle of $\Delta\theta = \pm 0.27°$ in the sky, and terrestrial solar radiation has a large diffuse component due to atmospheric scattering.[28] Figure 6a and b illustrate the simulated optical intensity profile of the fabricated diffractive element under normal incidence and under collimated light at $\theta = +1°$ from normal, respectively (the incident wavefronts have no k-vector component along the y-axis). For clarity, only the photons in the visible band from 360 to 760 nm are included, and the color of the profile indicates the wavelengths that have the greatest flux in a given region of space. At normal incidence, the diffractive element concentrates most of the visible light into the correct cell, with the shorter wavelengths (blue) focused onto the middle of the cell, while the longer wavelengths (red) closer to the cutoff of 760 nm lie at the boundary between the two cells. At $\theta = +1°$, all of the diffracted wavefronts undergo a shift in angle, so that the entire field at the image plane undergoes a lateral shift. This causes some of the visible light to leak into the infrared cell, starting with the wavelengths near the cutoff.

The spectral-splitting efficiency of the fabricated sample is shown in Figure 6c for several values of the incidence angle. Due to the predictable shift in the image with changing θ, the portion of the solar spectrum received by the two cells dramatically changes with incidence angle. With a large enough θ, the two spectral bands will almost fully illuminate the wrong cells. This reversal occurs when the image shifts by half the length of a unit cell, at an angle set by the structure's geometric aspect ratio (lateral period to vertical height): $\theta_{rev} = \tan^{-1}(0.5\ \text{mm}/13.7\ \text{mm}) = 2.1°$. Indeed, the measured spectral-splitting efficiency at $\theta = 2°$ is found to be approximately 28.9%, which is close to 100% minus the efficiency at normal incidence. At an angle of $\theta_{rev}/2$, roughly half of each spectral band should illuminate the correct cell, so that the spectral-splitting efficiency should be ∼50%. This is also seen in the experiment, where the spectral-splitting efficiency at $\theta = 1°$ is 48.4%. Since a splitting efficiency of 50% is equivalent to no splitting, the angular acceptance of the structure is limited to ca. ±1°. The angular response of the sample is thus robust enough to split direct unscattered sunlight with little loss in efficiency (see Supporting Information), while diffuse radiation is not rejected but is randomly dispersed between the cells and is therefore partially collected. We have considered here only light with no k-vector along the y-axis; since there are no variations in both the sample and image plane along the y direction, the efficiency has no significant dependence on angular shifts along this dimension.

We evaluate the utility of our spectral-splitting device under direct solar illumination by using detailed-balance methods to calculate the photovoltaic efficiency.[1] The periodically tiled structure in Figure 1a with two independently connected PV subcells is considered. Each subcell receives a modified version of the solar spectrum due to the dispersive properties of the phase mask. To find the spectrum of sunlight incident on each cell after passing through the phase mask, we simulate the response of the fabricated structure in Figure 3c over the full extent of the direct AM1.5D spectrum (280−4000 nm).[25] We assume that the phase mask is fully transmissive, and we neglect the small loss in splitting efficiency over the solar disk ($\theta = 0°$ to 0.27°). We further assume that the subcells have ideal step-function absorption spectra, and we work in the limit that both subcells have 100% external luminescence efficiency. Deviations from this limit, as well as further details on this calculation, are discussed in the Supporting Information.

Given these assumptions, the detailed-balance photovoltaic efficiency of the two-junction system under the AM1.5D

DOI: 10.1021/acsphotonics.6b00066
ACS Photonics 2016, 3, 886−894

spectrum is 36.5%. The optimal choice of band gaps for this system is 1.64 eV for the visible subcell (corresponding to the 760 nm cutoff in our optical design) and 1.12 eV for the infrared subcell. If we remove the degradations to the optical performance due to fabrication errors and use the optimal phase mask structure in Figure 3a for this calculation, the photovoltaic efficiency improves to 40.4%. The optimal band gaps for this case are 1.64 and 0.95 eV. The efficiency gain originates mostly from the increased sharpness of the spectral-splitting response of the optimized phase mask, which enhances absorption near the band edge of the visible subcell, where the photons are most efficiently utilized. Meanwhile, the infrared subcell shifts to a lower band gap due to a greater splitting efficiency for wavelengths longer than 1100 nm. The large difference between the fabricated and the optimized structures suggests that improvements in the efficiency of the spectral-splitting optics, especially in the spectral sharpness, have a significant impact on the efficiency of the photovoltaic system under direct sunlight. A benefit that is not reflected in these calculations is the increased robustness of the system's photovoltaic efficiency to solar spectrum variations (relative to a series-connected two-junction cell) owing to the independent connections to the subcells allowed by the lateral spectrum splitting structure.[3]

Further optimization of the design can improve the spectral-splitting efficiency of the structure in Figure 3b. For the same sample size of 1 mm, a reduction in pixel size can increase the efficiency by adding more degrees of freedom to the structure, while allowing the diffracted light to bend at sharper angles. By increasing the geometric aspect ratio, the angular acceptance can also be expanded, significantly improving the tolerance of the optical response to angular errors in solar tracking (see Supporting Information). However, a pixel size reduction does not fundamentally change the image-shifting angular response of the diffractive element, and the pixel size cannot be reduced indefinitely without changing the physics of the dielectric structure so that it no longer operates by diffraction. For instance, when the pixel size is smaller than a wavelength, resonances can be excited in the device,[10,29] and entirely new design strategies will be needed. Therefore, simply scaling the device in this direction cannot yield a substantial improvement in the angular acceptance.

Reductions in the pixel size still have the potential to improve the spectral-splitting efficiency under direct sunlight, and increasing the pixel aspect ratio allows the photovoltaic system to be made more compact. Furthermore, the ability of more tightly packed pixels to diffract light at sharper angles dramatically improves the efficiency of splitting incident light to three or more PV cells with different band gaps. To allow for these design improvements, the fabrication process must be improved to faithfully reproduce the optimized multilevel structure while allowing for better lateral and vertical resolution. Alternative fabrication methods can also be considered as the structure is scaled for large-area photovoltaics. Nanoimprint lithography[30] is an appealing option that has also been proposed for the fabrication of dielectric nanostructures on PV cells for light management.[10] With this method, a hard mask of the design (made using direct laser writing or electron-beam lithography) may potentially be patterned over many dielectric or polymer surfaces at high throughput. We do note that the adjoint method is fully compatible with three or more PV cells and diffractive designs based on smaller pixels.

CONCLUSION

Using computational optimization, we designed a thin dielectric optical element that splits the visible and near-infrared bands of the solar spectrum. Although specific spectral bands (with a cutoff at 760 nm) were chosen for our optimized structure, the adjoint method allows new designs to be rapidly generated with a different desired spectral response. Thus, our inverse design algorithm readily accommodates arbitrary illumination conditions or choice of photovoltaic materials. In the same vein, complexity can be added to the design (e.g., more, smaller design pixels or a new figure of merit) without incurring any significant computational cost. The dielectric optical elements were fabricated using femtosecond direct laser writing over large areas of several square millimeters, and measurements of the performance show good agreement with simulations. Improvements in fabrication methods to accurately produce feature sizes in the range of 1 μm may enable significant improvements in performance under direct sunlight, while also allowing for a more compact geometry and the incorporation of more PV subcells.

METHODS

Sample Fabrication. A glass slide was used as a substrate. The sample is fabricated by a direct laser writing system (Photonic Professional GT, Nanoscribe, Eggenstein-Leopoldshafen, Germany) using IP-Dip photoresist from Nanoscribe. The design was fabricated by using a dip-in technology. The final structure consists of numerous fields stitched next to each other. Each field has a size of 150 × 150 μm^2 and is fabricated layer-by-layer. The layers are separated by 400 nm. In each layer the scan lines are separated by 250 nm. The horizontal movement is carried out by laterally scanning the laser focus by galvanometric mirrors, whereas the vertical movement is carried out by piezo actuators. Each line is written with a scan speed of 50 mm/s.

Characterization Setup. The schematic of the setup is shown in Figure 4c. For the light source, a fiber-coupled tungsten halogen lamp with a wavelength range of 360 to 2400 nm was used (HL-2000, Ocean Optics, Dunedin, FL, USA). The light passes through a 75 mm focal length achromatic lens (49−538, Edmund Optics, Barrington, NJ, USA), reflects off of a silver mirror, and finally passes through an in-house-fabricated aperture matching the sample size. The transmitted light is collected with a fiber (numerical aperture of 0.22, which yields an acceptance angle of 12.7° in air) coupled Si photodiode array spectrometer (USB2000+, Ocean Optics) that covers the 380 to 970 nm wavelength range. Ten scans were used to improve signal-to-noise ratio. Background noise was subtracted within the manufacturer's software.

Instrument. Height values of the sample were determined by a dual confocal laser scanning microscope (OLS4100, Olympus, Waltham, MA, USA) using a 50× objective.

ASSOCIATED CONTENT

Supporting Information

The Supporting Information is available free of charge on the ACS Publications website at DOI: 10.1021/acsphotonics.6b00066.

Additional details on the optimization method and additional device characterization data (PDF)

DOI: 10.1021/acsphotonics.6b00066
ACS Photonics 2016, 3, 886−894

AUTHOR INFORMATION

Corresponding Authors

*E-mail (E. Yablonovitch): eliy@eecs.berkeley.edu.
*E-mail (P. V. Braun): pbraun@illinois.edu.

Present Address

#Magic Leap, Inc., 2189 Leghorn Street, Mountain View, California 94043, United States.

Author Contributions

□T. P. Xiao and O. S. Cifci contributed equally to this work.

Notes

The authors declare no competing financial interest.

ACKNOWLEDGMENTS

T.P.X. was supported by The Dow Chemical Company and the National Science Foundation Graduate Research Fellowship Program under Grant No. DGE 1106400. Transmission spectroscopy by O.S.C. was supported by the U.S. DOE "Light-Material Interactions in Energy Conversion" Energy Frontier Research Center under grant DE-SC0001293. O.S.C. is also grateful for financial support from the Turkish Ministry of Education. T.P.X. and E.Y. also acknowledge support from the U.S. DOE Bay Area Photovoltaics Consortium under grant DEEE0004946. T.G. and H.G. acknowledge support from BMBF, DFG, ERC (Complexplas), Zeiss- Foundation, and the BW-Stiftung. P.V.B. also acknowledges support from BW Stiftung (Spitzenforschung) as well as from the Alexander-von-Humboldt Foundation (Bessel Prize).

REFERENCES

(1) Shockley, W.; Queisser, H. J. Detailed Balance Limit of Efficiency of *p-n* Junction Solar Cells. *J. Appl. Phys.* **1961**, *32*, 510−519.
(2) Green, M. A.; Emery, K.; Hishikawa, Y.; Warta, W.; Dunlop, E. D. Solar Cell Efficiency Tables (version 46). *Prog. Photovoltaics* **2015**, *23*, 805−812.
(3) Warmann, E. C. Design Strategies for Ultra-high Efficiency Photovoltaics. Ph.D. Thesis, California Institute of Technology, Pasadena, CA, 2014.
(4) Torrey, E. R.; Ruden, P. P.; Cohen, P. I. Performance of a split-spectrum photovoltaic device operating under time-varying spectral conditions. *J. Appl. Phys.* **2011**, *109*, 074909.
(5) Broderick, L. Z.; Albert, B. R.; Pearson, B. S.; Kimerling, L. C.; Michel, J. Solar spectral variations and their influence on concentrator solar cell performance. *Proc. SPIE* **2013**, *8821*, 88210I-1−88210I-7.
(6) Stefancich, M.; Zayan, A.; Chiesa, M.; Rampino, S.; Roncati, D.; Kimerling, L.; Michel, J. Single element spectral splitting solar concentrator for multiple cells CPV system. *Opt. Express* **2012**, *20*, 9004−9018.
(7) Barnett, A.; Kirkpatrick, D.; Honsberg, C.; Moore, D.; Wanlass, M.; Emery, K.; Schwartz, R.; Carlson, D.; Bowden, S.; Aiken, D.; Gray, A.; Kurtz, S.; Kazmerski, L. Very High Efficiency Solar Cell Modules. *Prog. Photovoltaics* **2009**, *17*, 75−83.
(8) Ingersoll, G. B.; Lin, D.; Leger, J. R. Experimental verification of spectral grating interference in multiplexed volume holograms employed as broadband dispersive elements for solar concentrators. *Proc. SPIE* **2013**, *8821*, 882107-1−882107−11.
(9) Eisler, C. N.; Kosten, E. D.; Warmann, E. C.; Atwater, H. A. Spectrum splitting photovoltaics: polyhedral specular reflector design for ultra-high efficiency modules. *IEEE Photovoltaic Spec. Conf., 39th* **2013**, 1848−1851.
(10) Brongersma, M. L.; Cui, Y.; Fan, S. Light management for photovoltaics using high-index nanostructures. *Nat. Mater.* **2014**, *13*, 451−460.
(11) Levy, U.; Marom, E.; Mendlovic, D. Simultaneous multicolor image formation with a single diffractive optical element. *Opt. Lett.* **2001**, *26* (15), 1149−51.
(12) Kim, G.; Dominguez-Caballero, J.-A.; Lee, H.; Friedman, D. J.; Menon, R. Increased Photovoltaic Power Output via Diffractive Spectrum Separation. *Phys. Rev. Lett.* **2013**, *110*, 123901.
(13) Kim, G.; Dominguez-Caballero, J.-A.; Menon, R. Design and analysis of multi-wavelength diffractive optics. *Opt. Express* **2012**, *20*, 2814−2823.
(14) Shokooh-Saremi, M.; Magnusson, R. Particle swarm optimization and its application to the design of diffraction grating filters. *Opt. Lett.* **2007**, *32*, 894−896.
(15) Johnson, E. G.; Abushagur, M. A. G. Microgenetic-algorithm optimization methods applied to dielectric gratings. *J. Opt. Soc. Am. A* **1995**, *12*, 1152−1160.
(16) Miller, O. D. Photonic Design: From Fundamental Solar Cell Physics to Computational Inverse Design. Ph.D. Thesis, University of California, Berkeley, CA, 2012.
(17) Lalau-Keraly, C. M.; Bhargava, S.; Miller, O. D.; Yablonovitch, E. Adjoint shape optimization applied to electromagnetic design. *Opt. Express* **2013**, *21*, 21693−21701.
(18) Scranton, G.; Bhargava, S.; Ganapati, V.; Yablonovitch, E. Single spherical mirror optic for extreme ultraviolet lithography enabled by inverse lithography technology. *Opt. Express* **2014**, *22*, 25027−25042.
(19) Ganapati, V.; Miller, O. D.; Yablonovitch, E. Light trapping textures designed by electromagnetic optimization for subwavelength thick solar cells. *IEEE J. Photovolt.* **2014**, *4* (1), 175−182.
(20) Piggott, A. Y.; Lu, J.; Lagoudakis, K. G.; Petykiewicz, J.; Babinec, T. M.; Vučković, J. Inverse design and demonstration of a compact and broadband on-chip wavelength demultiplexer. *Nat. Photonics* **2015**, *9*, 374−377.
(21) Goodman, J. W. *Introduction to Fourier Optics*, 2nd ed.; McGraw-Hill: New York, 1996.
(22) Poynting, J. On the Transfer of Energy in the Electromagnetic Field. *Philos. Trans. R. Soc. London* **1884**, *175*, 343−361.
(23) Lorentz, H. A. The theorem of Poynting concerning the energy in the electromagnetic field and two general propositions concerning the propagation of light,. *H. A. Lorentz Collected Papers* **1896**, *3*, 1−11.
(24) Nocedal, J.; Wright, S. J. *Numerical Optimization*, 2nd ed.; Springer: New York, 1999.
(25) National Renewable Energy Laboratory. Reference Solar Spectral Irradiance: Air Mass 1.5, ASTM G-173−03. http://rredc.nrel.gov/solar/spectra/am1.5 (accessed Aug 15, 2015).
(26) Fischer, J.; Wegener, M. Three-dimensional optical laser lithography beyond the diffraction limit. *Laser Photonics Rev.* **2013**, *7*, 22−44.
(27) Thorlabs, Inc. C120 Compact Photodiode Power Head with Silicon Detector. http://www.thorlabs.com/thorcat/18300/S120C-SpecSheet.pdf (accessed October 17, 2015).
(28) Erbs, D. G.; Klein, S. A.; Duffie, J. A. Estimation of the diffuse radiation fraction for hourly, daily and monthly-average global radiation. *Sol. Energy* **1982**, *28*, 293−302.
(29) Chang-Hasnain, C. J.; Yang, W. High-contrast gratings for integrated optoelectronics. *Adv. Opt. Photonics* **2012**, *4*, 379−440.
(30) Chou, S. Y.; Krauss, P. R.; Renstrom, P. J. J. Nanoimprint lithography. *J. Vac. Sci. Technol., B: Microelectron. Process. Phenom.* **1996**, *14*, 4129−4133.

DOI: 10.1021/acsphotonics.6b00066
ACS Photonics 2016, 3, 886−894